The Astrophysical Journal, 618:385–396, 2005 January 1

RADIAL DISTRIBUTION OF DUST GRAINS AROUND HR 4796A

Z. Wahhaj,[1,2] D. W. Koerner,[2,3] D. E. Backman,[4] M. W. Werner,[3,5] E. Serabyn,[6] M. E. Ressler,[3,5] and D. C. Lis[6]
Received 2004 June 18; accepted 2004 September 9

ABSTRACT

We present high dynamic range images of circumstellar dust around HR 4796A that were obtained with MIRLIN at the Keck II telescope at $\lambda = 7.9$, 10.3, 12.5, and 24.5 μm. We also present a new continuum measurement at 350 μm obtained at the Caltech Submillimeter Observatory. Emission is resolved in Keck images at 12.5 and 24.5 μm with point-spread function FWHM values of 0.″37 and 0.″55, respectively, and confirms the presence of an outer ring centered at 70 AU. Unresolved excess infrared emission is also detected at the stellar position and must originate well within 13 AU of the star. A model of dust emission fitted to flux densities at 12.5, 20.8, and 24.5 μm indicates that dust grains are located 4^{+3}_{-2} AU from the star with effective size 28 ± 6 μm and an associated temperature of 260 ± 40 K. We simulate all extant data with a simple model of exozodiacal dust and an outer exo-Kuiper ring. A two-component outer ring is necessary to fit both Keck thermal infrared and *Hubble Space Telescope* scattered-light images. Bayesian parameter estimates yield a total cross-sectional area of 0.055 AU^2 for grains roughly 4 AU from the star, and an outer-dust disk composed of a narrow large-grain ring embedded within a wider ring of smaller grains. The narrow ring is 14 ± 1 AU wide with inner radius 66 ± 1 AU and total cross-sectional area 245 AU^2. The outer ring is 80 ± 15 AU wide with inner radius 45 ± 5 AU and total cross-sectional area 90 AU^2. Dust grains in the narrow ring are about 10 times larger and have lower albedos than those in the wider ring. These properties are consistent with a picture in which radiation pressure dominates the dispersal of an exo-Kuiper belt.

Subject headings: circumstellar matter — infrared: stars — planetary systems: formation — planetary systems: protoplanetary disks — solar system: formation — stars: individual (HR 4796A)

1. INTRODUCTION

In the last half-decade, advances in high-resolution long-wavelength techniques have yielded an increased number of spatially resolved images of thermal emission from dusty disks around nearby stars (Greaves et al. 1998; Holland et al. 1998, 1999; Jayawardhana et al. 1998 [hereafter J98]; Koerner et al. 1998 [hereafter K98], 2001; Wilner et al. 2002; Wahhaj et al. 2003; Weinberger et al. 2003). These typically reveal dust masses located at several tens of AU from the central star in a region analogous to the Edgeworth-Kuiper belt in our own solar system. In most instances, emission is markedly reduced close to the star. This inner clearing was previously inferred in some cases on the basis of the spectral energy distribution (SED) (e.g., Jura et al. 1998). Dust located here is most easily detected at mid-infrared (MIR) wavelengths, where stellar photospheric radiation is relatively diminished and circumstellar dust emission is at a maximum. If located within an ice condensation radius, it can be considered analogous to the solar system's zodiacal dust, a population of grains that emanates from asteroid collisions and the disintegration of comet tails (Dermott et al. 1994). The presence of such an "exozodiacal" dust component was inferred by K98 on the basis of high-resolution (~0.″4) 12 and 20 μm images of HR 4796A.

The detection of exozodiacal dust is of considerable importance to efforts aimed at the detection of Earth-like planets (Backman et al. 1998). In light of a rapid dispersal timescale ($<10^4$ yr; Gustafson 1994), current detections imply an origin in the collision of minor planetary bodies and perhaps resonant trapping by larger ones. The dust also may impact planetary detection techniques as a source of confusing radiation (Backman et al. 1998). Despite their importance, detections are currently few in number. Evidence for exozodiacal dust around HR 4796A was recently brought into question by Telesco et al. (2000, hereafter T00) and Li & Lunine (2003, hereafter LL03). Resolution of the issue is complicated by the fact that a prominent outer dust ring provides a confusing signature at the resolution of HR 4796A images. Here we present additional high-resolution images of HR 4796A with modeling designed to better understand the radial structure of its circumstellar dust, including whether or not an exozodiacal dust component is required by the data.

HR 4796A is an A0 V star (Houk & Sowell 1985) located at a distance of 67 ± 3 AU (*Hipparcos* catalog) with an age of 8 ± 2 M yr (Stauffer et al. 1995). K98 and J98 first resolved the disk in thermal infrared (IR) images. J98 noted that a line cut through their 18 μm image could be simulated with a ring 50–110 AU in extent. K98 simulated Keck images at higher resolution and demonstrated over a large range of models that an inner clearing was demanded by the data. The most probable values of disk properties yielded inner and outer radii of 55 and 80 AU, respectively, for a disk inclined ~73° from face-on. K98 also found excesses at the stellar position at 12 and 20 μm with values that implied a dust temperature of ~250 K and, in

[1] University of Pennsylvania, David Rittenhouse Laboratory, 209 South 33rd Street, Philadelphia, PA 19104-6396.
[2] Northern Arizona University, Department of Physics and Astronomy, Building 19, Room 209, Flagstaff, AZ 86001-6010.
[3] Visitors to the W. M. Keck Observatory, 65-1120 Mamalahoa Highway, Kamuela, Hawaii 96743.
[4] Physics and Astronomy Department, Franklin and Marshall College, P.O. Box 3003, Lancaster, PA 17604.
[5] Jet Propulsion Laboratory, California Institute of Technology, 4800 Oak Grove Drive, Pasadena, CA 91109.
[6] Division of Physics, Mathematics, and Astronomy, California Institute of Technology, Pasadena, CA 91125.

TABLE 1
Flux Densities for HR 4796A

$\lambda_{\rm eff}$ (μm)	$\delta\lambda$ (μm)	Flux Density (Jy)	Uncertainty (Jy)	Photosphere (Jy)	Reference
7.9	0.87	0.307	0.044	0.283	1
10.3	1.01	0.218	0.024	0.168	1
12.5	1.16	0.231	0.014	0.114	1
20.8	1.00	1.62	0.16	0.041	1
24.5	0.8	2.1	0.17	0.03	1
350.0	...	0.160	0.042	$\sim$0	1
10.8	5.3	0.188	0.047	0.152	2
18.2	1.7	0.905	0.130	0.054	2
18.2	1.7	1.100	0.150	0.054	3
20.0	...	1.860	0.186	0.045	4
800.0	100.	0.028	0.0093	$\sim$0	5
10.1	5.1	0.270	0.026	0.174	6
10.3	1.3	0.233	0.024	0.167	6
11.6	1.3	0.225	0.070	0.132	6
12.5	1.2	0.253	0.027	0.114	6
450.0	$\sim$30	0.180	0.150	$\sim$0	7
850.0	$\sim$50	0.0191	0.0034	$\sim$0	7
12.0	6.5	0.309	0.028	0.123	8
25.0	11	3.280	0.130	0.029	8
60.0	40	8.640	0.430	0.005	8
100.0	37	4.300	0.340	0.002	8

References.—(1) This work; (2) Telesco et al. 2000; (3) J98; (4) Jura et al. 1993; (5) Jura et al. 1995; (6) Fajardo-Acosta et al. 1998; (7) Holland et al. 1998; (8) *IRAS*.

turn, a location $\sim$4.5 AU from the star. Schneider et al. (1999, hereafter S99) imaged scattered light from the HR 4796A outer ring with the *Hubble Space Telescope* (*HST*) NICMOS and confirmed the presence of a narrow (17 AU) outer ring centered at 70 AU. T00 and Wyatt et al. (1999, hereafter W99) analyzed Keck images at 10 and 18 μm and derived a radial surface density to the outer ring that rose exponentially from $\sim$45 AU, doubled between 60 and 70 AU, and fell $\propto r^{-3}$ outside 70 AU with an outer cutoff at $\sim$130 AU. Grain sizes were estimated to be 2–3 μm, in contrast to the 30 μm grains found by K98. T00 also found that any excess detected in their images at the stellar position was consistent with their photometric uncertainties. Augereau et al. (1999) presented models of the SED of HR 4796A that predicted dust within 10 AU of the star. LL03 showed that the SED could be modeled without a zodiacal dust component. Sitko et al. (2000) observed that the silicate emission feature is very weak, suggesting that there are not many small silicate grains near the star. He also estimated that only half the flux in the 8–13.5 μm range is photospheric, detecting more excess than in the 12.5 μm MIRLIN image in K98. Here we present new data and model all extant measurements simultaneously. These allow us to resolve disputes about the properties of dust around HR 4796A.

2. OBSERVATION

HR 4796A was observed on UT 1998 June 11 and 14, 1999 January 30, and 1999 February 3 with the MIR camera MIRLIN at the Keck II telescope. MIRLIN's detector is a Boeing 128 pixel $\times$ 128 pixel, high-flux Si : As BIB array with a Keck II plate scale of 0.″138 pixel^{-1} and a 17.″5 field of view (Ressler et al. 1994). Chopping with the Keck II secondary mirror was carried out in a north-south direction at a 4 Hz rate with a throw of 7″. Between chop sequences, the telescope was nodded east-west with a similar throw. Since thermal IR emission from HR 4796A is confined to within a maximum length of 5″, the 7″ chop/nod throw was sufficient for differencing of any pair of images without overlap. Observations were carried out in filters centered at $\lambda = 7.9$, 10.3, 12.5, and 24.5 μm with widths of 0.76, 1.01, 1.16, and 0.76 μm, and for on-source integration times of 3, 6, 6, and 52 minutes, respectively. Images on double-differenced frames were cross-correlated with a point-spread function (PSF) to determine a first estimate of the centroid position and were then co-added. The resulting image was then used in place of the PSF to repeat the process with improved centroiding and to produce a new stacked image. This procedure was repeated multiple times until there was no perceptible change in the final co-added image on successive iterations. The final image was sized to 64 pixels $\times$ 64 pixels (8.″8 $\times$ 8.″8) to optimally window the emission from HR 4796A and the adjacent background. Infrared standards β Leo, 2 Cen, α Sco, and α Boo were observed in the same way at 7.9 (and 10.3), 12.5, 20.8, and 24.5 μm, respectively, at similar air masses.

To better constrain the properties of grains around HR 4796A, a new continuum measurement was obtained on UT 1998 May 23 at 350 μm with the SHARC linear bolometer array camera at the Caltech Submillimeter Observatory. Atmospheric conditions were good, with a steady τ_{225} of 0.36. The flux calibrator was Uranus, with an angular size of 3.″59 and a flux density of 242 Jy on that date. The resulting 350 μm flux density of HR 4796A was observed to be 160 ± 42 mJy and is listed in Table 1.

Images of HR 4796A are unresolved at $\lambda = 7.9$ and 10.3 μm with respective PSF FWHM values of 0.″48 and 0.″45 and are not displayed here. Flux densities were calculated by comparison with images of β Leo obtained shortly after those of HR 4796A. Flux densities of 307 ± 44 and 218 ± 24 mJy at 7.9 and 10.3 μm were derived, assuming values of 10.68 and 6.44 Jy for β Leo at the same wavelengths (Koerner et al. 2000). Photospheric estimates 283 mJy at 7.9 μm and 168 mJy at 10.3 μm were derived by the fit of a model A0 V star (Kurucz 1993) to measurements of HR 4796A at wavelengths shorter than 3 μm. It

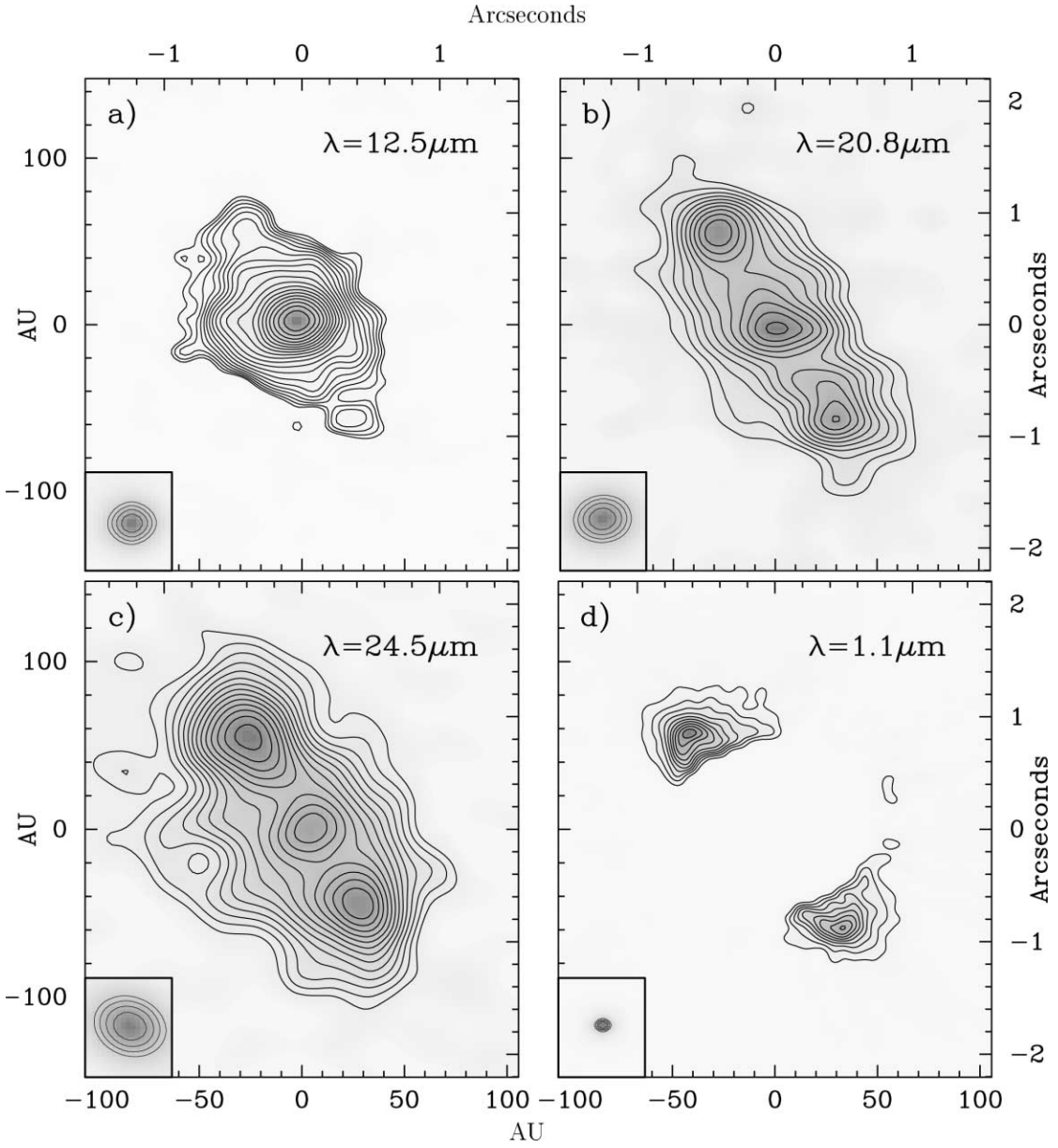

FIG. 1.—KECK/MIRLIN contour maps of HR 4796A from new observations at thermal IR wavelengths and the *HST*/NICMOS image from S99. North is aligned with the up position. Contour images of the PSF stars, 2 Cen, α Sco, and α Boo, are displayed in (*a*)–(*c*) as insets with contour intervals of 10%, starting at the 60% level. The inset in (*d*) shows a Tiny Tim PSF at the resolution (0.″12) of the *HST*/NICMOS observation at $\lambda = 1.1$ μm. The contour levels for the inset in (*d*) are the same as in the other panels. (*a*) Emission at $\lambda = 12.5$ μm. Lowest contour is at the 2 σ level (32 mJy arcsec^{-2}). Higher contour levels are at 2 $\sigma \times (10^{0.068n})$ for the nth contour. (*b*) Emission at $\lambda = 20.8$ μm with 1 σ (47 mJy arcsec^{-2}) contour intervals and contours starting at the 2 σ level. (*c*) Emission at $\lambda = 24.5$ μm contoured as in (*b*) with 1 $\sigma = 39$ mJy arcsec^{-2}. (*d*) Scattered light at $\lambda = 1.1$ μm. This observation of HR 4796A was made with *HST*/NICMOS (S99) at 1.1 μm. The NICMOS coronagraph was used to mask the star at the center of the image. Scattered light within 0.″6 of the star was deemed artifactual and is not shown in this image. The lowest contour is at 2 σ (1.8 mJy arcsec^{-2}), and successive contours are drawn at 2 σ intervals.

seems that there is a small excess at 10.3 μm and an even smaller excess, or possibly none, at 7.9 μm.

The 12.5 μm image is shown in Figure 1*a*. The 64×64 image was finely gridded to 256 pixels $\times$ 256 pixels and then smoothed by convolution with a circular hat function of radius equal to the FWHM of α Boo (PSF star), which was observed immediately after HR 4796A. The resolution of the image is 0.″37. Peak brightnesses are calculated as the flux in the brightest pixel, divided by the pixel area. The central peak brightness was measured to be 723 ± 44 mJy arcsec^{-2}, while that expected from the photosphere is 387 mJy arcsec^{-2}. The total flux at 12.5 μm is 231 ± 14 mJy, while the photospheric flux at 12.5 μm is 114 mJy. The long axis enclosed by the 3 σ contour is 2.″1 (141 AU). Northeast and southwest peaks are detected with total separation 1.″9 (127 AU). The northeast and southwest peaks are not equal in brightness but have a flux ratio of 1.13.

The 20.8 μm image displayed in Figure 1*b* is a rereduced version of data presented in K98. Shifting and adding was carried out as described above, starting with a model of the emission derived from earlier versions of the image. The result exhibits improved S/N and a flux density, 1.62 ± 0.16 Jy, that is consistent with the previously reported 1.88 ± 0.17 Jy. The final shift-and-add image was smoothed to match the 0.″4 resolution of the other images in Figure 1. Emission peaks northeast and southwest of the star are separated by 1.″85 (124 AU) in the final smoothed image. The central peak is brightest and 0.″93 (62 AU) from the southwest peak and the same distance from the northeast peak. Peak brightness values are 629, 668, and

623 mJy arcsec^{-2} at the northeast, center, and southwest positions, respectively. The photospheric flux at $\lambda = 20.8$ μm is 41 mJy, which corresponds to a peak brightness of at most 82 mJy arcsec^{-2}.

The 24.5 μm image is shown in Figure 1*c* and was reduced in the same way as the 12.5 μm image with α Boo used as the PSF star. Image resolution was 0.″55. The expected flux from the photosphere is 30 mJy, while the total measured flux for HR 4796A was 2100 ± 170 mJy. The expected photospheric brightness in the peak pixel is at most 44 mJy arcsec^{-2}. Comparing this to the central peak brightness of 585 mJy arcsec^{-2}, it is immediately obvious that most of the emission in the central pixel is nonphotospheric and probably the result of hot circumstellar dust. The emission extends 1.″68 (113 AU) from the northeast peak to the southwest peak. The extent of the 3 σ contour is 3.″6 (242 AU). The central peak is 0.″74 (50 AU) from the southwest peak and 0.″94 (63 AU) from the northeast peak. Peak brightnesses are 637, 617, and 585 mJy arcsec^{-2} at the northeast, southwest, and central positions, respectively. The northeast/southwest brightness ratio is 637:617 = 1.04.

A very high resolution image of light scattered by the HR 4796A ring was obtained by S99 with the NICMOS coronagraphic camera on board *HST*. We have contoured the 1.1 μm image and displayed it in Figure 1*d* for comparison to the thermal IR images. The region within 0.″6 of the star has artifactual emission from coronagraphic scattering and has been masked off. At a resolution of 0.″12 (8 AU), the emission is extended 2.″06 (138 AU) from the northeast to the southwest peak and exhibits a brightness asymmetry (northeast : southwest) of 14.4:12.2 = 1.18. The extent of the 2 σ contour line is much more confined than in the thermal IR images.

The images in Figure 1 confirm the general properties of ring emission inferred from previous high-resolution images (K98; S99; T00). Flux density measurements at the stellar position also appear to substantiate earlier evidence for a hot dust component close to the star (K98). The latter interpretation requires careful consideration, however, since the highly inclined ring passes within 0.″3 of the star, and the PSF FWHM is 0.″4. It is necessary to carefully account for the contribution of ring emission at the stellar position to identify the presence of hot dust near the star with certainty. In addition, the structure of the ring itself may be better ascertained with detailed analyses that combine information from all images. To accomplish both goals, we compare a variety of ring models to the Keck/MIRLIN and *HST* images.

3. MODELING

Our modeling approach is designed to best interpret all available observations of HR 4796A, including optical and thermal IR images and flux densities at longer wavelengths. As a first step, we examine individual Keck/MIRLIN images for evidence of dust close to the star. Then we quantitatively compare models of dust emission by fitting them simultaneously to all available data. To successfully deduce key disk properties in this manner, it is necessary to strike a balance between the need for a detailed physical description (including grain shape, size, and composition) and an appropriate number of free parameters. To best achieve this compromise, we use a simple model of emission from a flat, optically thin disk as described in Backman et al. (1992). It will be evident from the modeling process that further complications in disk structure, such as a flared disk or a disk with a thick inner edge, are not required at the resolution of extant data. According to the Backman et al. model, thermal radiation from an annulus of width dr at distance r from the star is

$$f_t(r) = (1-\omega)\sigma(r)\epsilon_\lambda B[T_p(r),\ \lambda]\left(\frac{2\pi r dr}{D^2} sr\right) \text{ Jy},$$

where $\sigma(r)$ is the fractional surface density, $T_p(r)$ is the grain temperature, and D is the distance to HR 4796A, 67 pc. The optical depth is defined as $\tau(r,\nu) = (1-\omega)\sigma(r)\epsilon_\lambda$, where ω is the albedo. For moderately absorbing dielectrics and an effective grain radius a, the radiative efficiency is $\epsilon_\lambda = 1.5a/\lambda$ for $\lambda > 1.5a$ and $\epsilon_\lambda = 1$ for $\lambda < 1.5a$ (Greenberg 1978). The grain temperature for efficient absorbers and inefficient emitters is $T_p(r) = 468(L_*/\lambda_0)^{0.2}(r/1\text{ AU})^{-0.4}$, as calculated from radiative balance equations (Backman & Paresce 1993); L_* is the stellar luminosity in solar units. The fragmentation process caused by inelastic collisions between large grains results in a steady-state size distribution described by $n(a) \sim a^{-3.5}$ (Dohnanyi 1969). It has been shown that the SED resulting from such a collisional cascade of grains can be approximated by the SED of a population of grains of a single size (Backman et al. 1992). The minimum grain radius in the distribution is $a_{\min} \sim a/4$, where a is the effective radius of the representative grains.

To simulate the *HST*/NICMOS image from S99 in Figure 1*d*, we use the following prescription for an emission model. The scattered-light emission from an annulus of width dr at distance r from the star is

$$f_s(r) = \omega\sigma(r)B_*(R_*/r)^2\left(\frac{2\pi r dr}{4D^2} sr\right) \text{ Jy},$$

where B_* and R_* are the surface intensity and radius of the star. It is important to note that grain size does not affect the intensity of scattered-light emission, as grain temperature is not a factor. Therefore, the grain radius a will not be a parameter in scattered-light modeling.

In keeping with simple theoretical expectations, models used to interpret low-resolution observations of debris disks often approximate the surface density σ as proportional to $r^{-\gamma}$, where r is the stellocentric distance (Gillett 1986; Diner & Appleby 1986; Nakano 1988; Artymowicz et al. 1989; Backman et al. 1992). High-resolution imaging has revealed a ringlike structure in many cases, however, necessitating the specification of other model parameters, such as inner and outer radii R_{in} and R_{out} and ring width ΔR.

To estimate photospheric emission from HR 4796A, we scale a model of the emission from an A0 V star by Kurucz (1993). Model fitting uses all available photometric measurements of HR 4796A at wavelengths shortward of 3 μm. To simulate images, the resulting photospheric flux density is used to scale a point source at the stellar position. As a first approximation, we then add emission from a single-ring model and convolve the entire image with an appropriate PSF star. As demanded by the data, we then consider the addition of multiple rings in a similar modeling process.

To calculate the range of acceptable values for model parameters as dictated by a simultaneous comparison to all data, we use a Bayesian approach that assigns a relative probability, $e^{-1/2\Sigma_n \chi_n^2}$, to each model. Here χ_n^2 refers to χ^2 as defined for the nth data set. This requires a consistent way of weighting χ^2 from the image fits with those from SED fits. Thus, for each image, all pixels of intensity above 3 σ are counted and divided

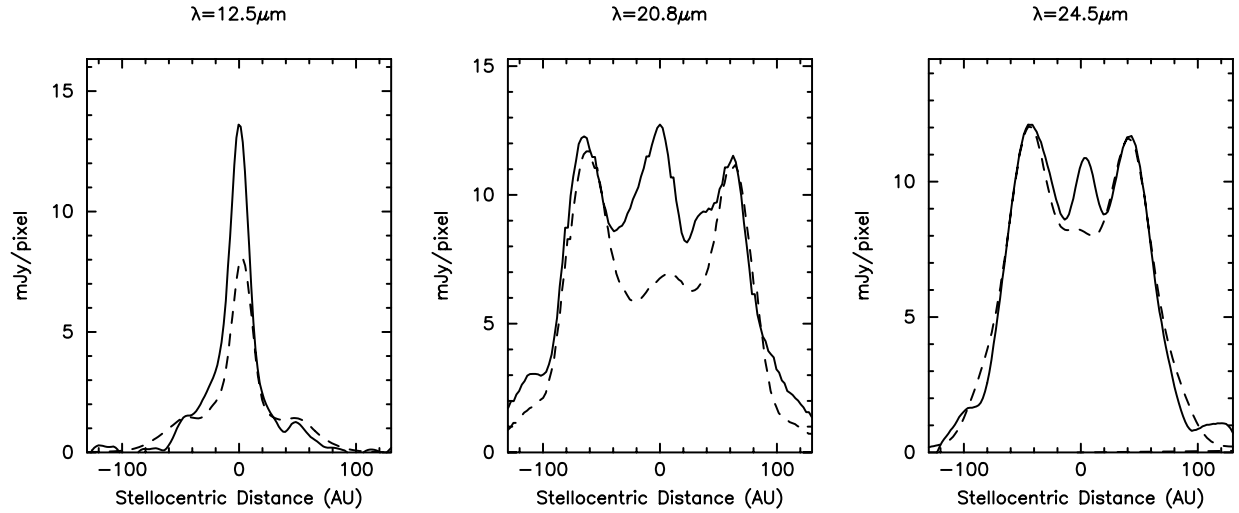

FIG. 2.—Models of stellar emission plus thermal emission from an outer ring scaled to match the outer disk's intensity are shown at 12.5, 20.8, and 24.5 μm. The solid lines represent line cuts through data. The dashed lines represent line cuts through thermal emission models of HR 4796A with a simple outer ring as described in the text. All line cuts have a P.A. of 26° and pass through both the northeast and southwest peaks of emission.

by the area (in pixels) enclosed by the half-maximum contour of the corresponding PSF. This gives a measure of the number of data points represented by an image. The χ^2 values from each of the image fits is normalized using this number.

Probabilities are calculated for models varying over a large parameter space, and the relative probability of a specific parameter value is derived by summing probabilities for all models with that value. In this way, probability distributions are built up for the values of each parameter (e.g., Lay et al. 1997). As a prelude to modeling the entire data set, we first consider the question of whether or not the images mandate the presence of material close to the star that is analogous to the solar system's zodiacal dust.

3.1. *Exozodiacal Dust*

To date, consensus is lacking in published interpretations of evidence for an inner zodiacal dust component to the HR 4796A system. K98 derived an IR excess at the stellar position by fitting a scaled PSF to high-resolution Keck images at 12.5 and 20.8 μm and comparing the results to expected photospheric levels. T00 failed to detect this excess at 18.2 μm, however, by carrying out a similar analysis on Keck images taken under nonideal photometric conditions. LL03 were able to fit the SED without an inner dust component by varying grain composition and using outer-disk constraints supplied by the 1.1 μm *HST* image (S99).

The contradiction implied by these results reflects the difficulty of the analysis. Thermal IR flux calibration is difficult from the ground, and the inner dust component is at the limit of available spatial resolution. For example, T00 derived a total flux density 20% lower than their previous measurement in the same filter at a different telescope (J98). If the latter measurement is in error, it would lead to an underestimate of the point-source excess after subtraction of flux from a photospheric model. It is also not surprising that LL03 did not find the case for inner dust compelling on the basis of SED shape alone, since the function that corresponds to emission at a given stellocentric distance is quite broad. The dust component inferred by K98 produces a negligible contribution to the overall SED and can be properly substantiated only by high-resolution *imaging* data. Keck thermal IR images of HR 4796A easily separate emission at the stellar position from that of the ring along the long axis of emission ($\theta \sim 1''$). However, the ring is oriented 27° from edge-on, and the observations have insufficient resolution across the minor axis ($\theta \leq 0''.25$). Consequently, simple PSF fitting will be subject to an uncertainty from contamination by outer-ring emission. Here we present a modeling approach that accounts for confusion from the outer ring in order to interpret new high-resolution images.

To make an estimate of the contribution of outer-ring radiation to flux detected at the stellar position, we first fit a simple model of outer-ring emission solely to the region outside of

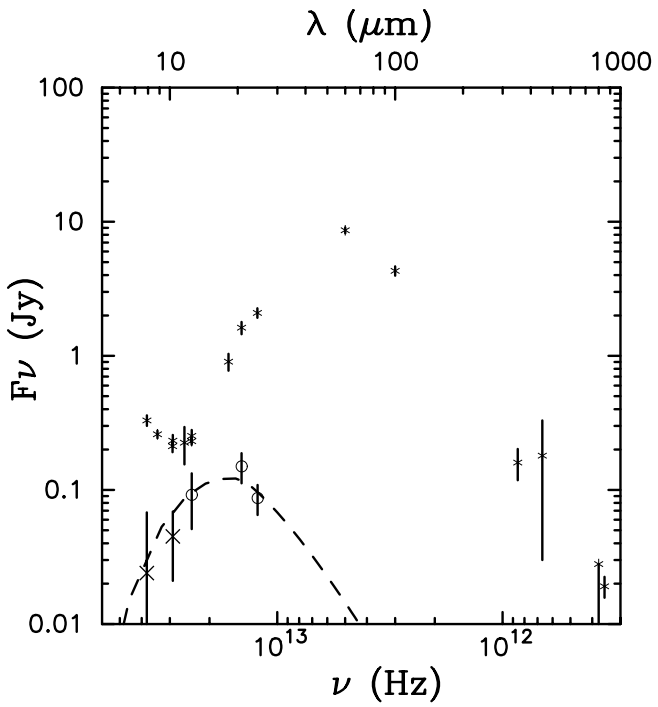

FIG. 3.—Photometry of HR 4796A from Table 1 are denoted as asterisks. Zodiacal excesses calculated from point-source fitting to images at $\lambda = 12.5$, 20.8, and 24.5 μm are shown as circles at the bottom left corner of the figure. Estimated flux densities from the zodiacal component at 10.3 and 7.9 μm are shown as crosses. The dashed line represents the simulated SED of a model fitted to the zodiacal excesses. This model was a dust ring ($T \sim 280$ K) with radius 3.3 AU, width 0.5 AU, grain radius 14 μm, and $\sigma = 0.0045$.

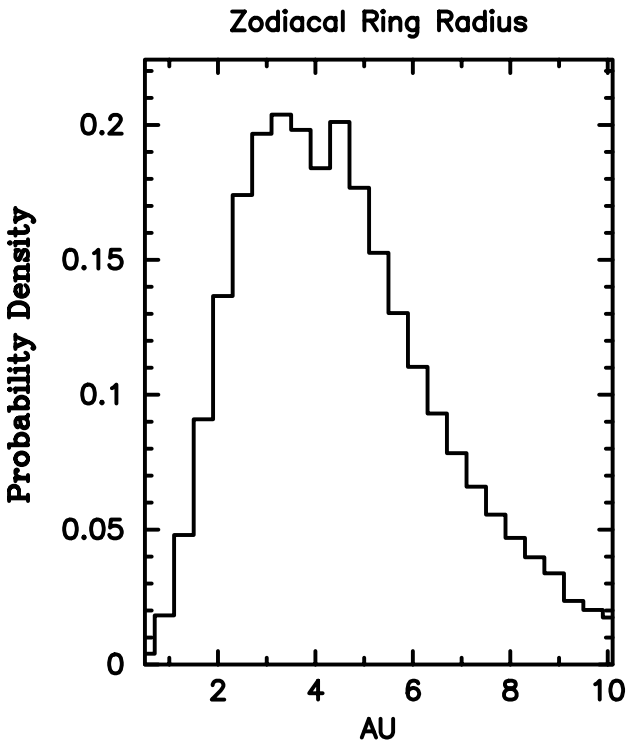

FIG. 4.—Probability distribution for the radius of the zodiacal ring obtained by the Bayesian approach. The best estimate for the radius is 4^{+3}_{-2} AU.

35 AU (0″.52) from the star. Our initial model was a single flat ring with density $\sigma(r) \sim r^{-\gamma}$, with the rotational axis inclined 73° to the line of sight (S99), and with the long axis aligned at position angle P.A. = 26°. A point source with photospheric flux density was added at the stellar position, and the entire model image was convolved with a PSF star. Ring parameters were varied in independent fits to each of the three images at $\lambda = 12.5,\ 20.8$, and 24.5 μm. Figure 2 shows line cuts through both the images and best-fit models. It is immediately evident that *in each case* these models fail to reproduce an adequate amount of emission at the stellar position. This comparison strongly supports the inference of an inner zodiacal dust component, as concluded by K98.

We make a quantitative estimate of the contribution of emission from inner dust by refitting our model to unmasked versions of the thermal IR images while varying the model flux density at the stellar position. Expected photospheric contributions of 114, 41, and 30 mJy at 12.5, 20.8, and 24.5 μm, respectively, were subtracted from the best-fit result to yield estimates of 92 ± 41, 150 ± 38, and 87 ± 22 mJy for the inner-component flux densities. The results are plotted in Figure 3. It is evident from Figure 3 that the inner component of dust contributes negligibly to the total SED at all wavelengths. Hence, the above result is consistent with the null result of LL03. As a first approximation to estimate physical properties of a zodiacal dust component, we assume that grains are located in a single ring of width 0.5 AU and vary the ring inner radius $r_{\rm in}$, surface density σ, and effective grain radius a. Best-fit values are $r_{\rm in} = 4^{+3}_{-2}$ AU, $\sigma = 0.0046 \pm 0.001$, and $a = 14 \pm 3$ μm, with uncertainties determined by the Bayesian approach described earlier. This implies an average grain temperature of 260 ± 40 K. Ice grains of this size in a gas-free environment would have to be at a radial separation of at least 43 AU to survive sublimation for any appreciable amount of time (Isobe 1970). To evaluate the consistency of our 10.3 and 7.9 μm photometry with this simulation, we also plot the estimated contribution to the inner component at these wavelengths in Figure 3. Assuming that the outer-ring SED can be approximated by a 110 K blackbody (Jura et al. 1998) and that at 12.5 μm the outer-ring contribution is ~25 mJy, we extrapolate the outer-ring contribution to be ~5 mJy at 10.3 μm and 0.2 mJy at 7.9 μm. Thus, the inner-component flux density is 45 ± 24 mJy at 10.3 μm and 24 ± 44 mJy at 7.9 μm. From Figure 3, it is evident that our zodiacal dust model can account for these excesses. We emphasize the approximate nature of this estimate and underscore the point that the actual dust configuration may be far more complicated. Nevertheless, a single-ring approximation yields a radial location as indicated in Figure 4, the probability distribution for the inner-ring radius. The uncertainty encloses the 66% confidence interval in the probability distribution.

It is evident in Figure 2 that the simple power-law description for $\sigma(r)$ in the outer ring fails beyond the outer-ring edge. We expect this discrepancy to have no effect on our estimate of the zodiacal dust component. However, we explore it below with a more detailed model to better understand outer-ring structure.

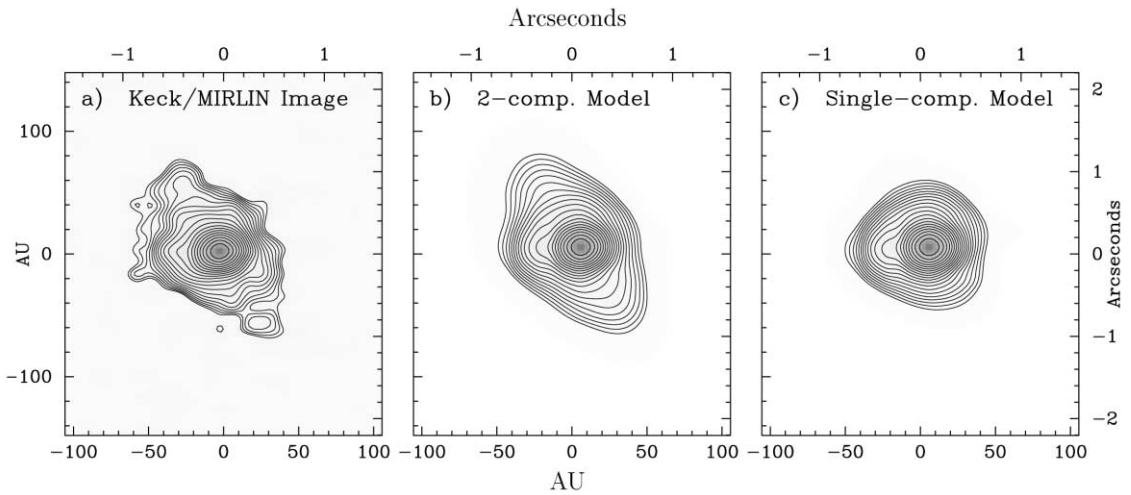

FIG. 5.—Comparison of (*a*) 12.5 μm image with simulations from (*b*) two-component outer-ring model and (*c*) a single outer-ring model. Both simulations are from best-fit models to all extant data. Contour levels are same as in Fig. 1*a*.

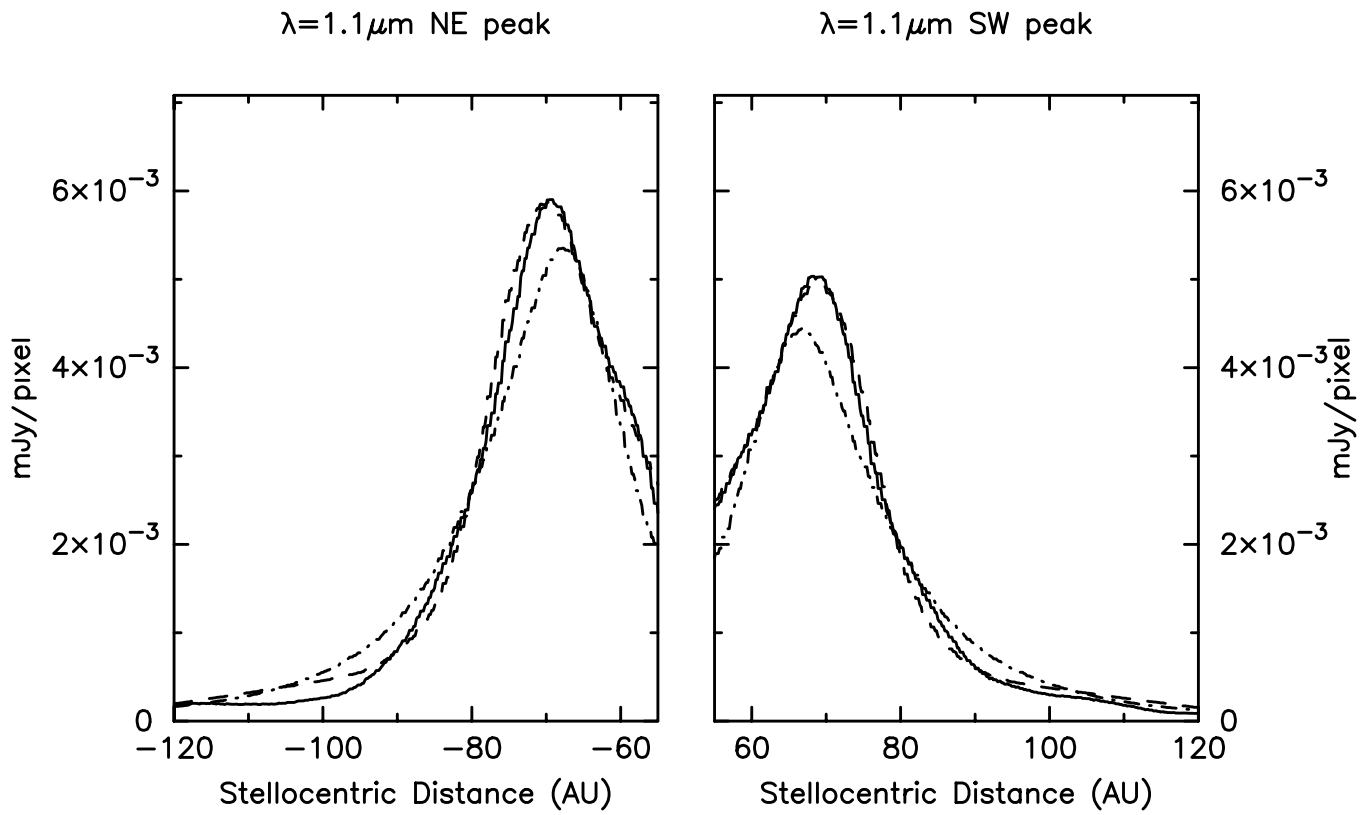

FIG. 6.—Strip cuts through the 1.1 μm *HST*/NICMOS image are shown as solid lines. Cuts through a simulated image from the two-component outer-ring model are shown as dashed lines. The dash-dotted line represents the single-component model. All 8 AU wide strip cuts are along a P.A. of 26° and pass through both northeast and southwest peaks of emission. The northeast portion is shown on the left, and the southwest portion is shown on the right. The section in between was masked by the NICMOS coronograph.

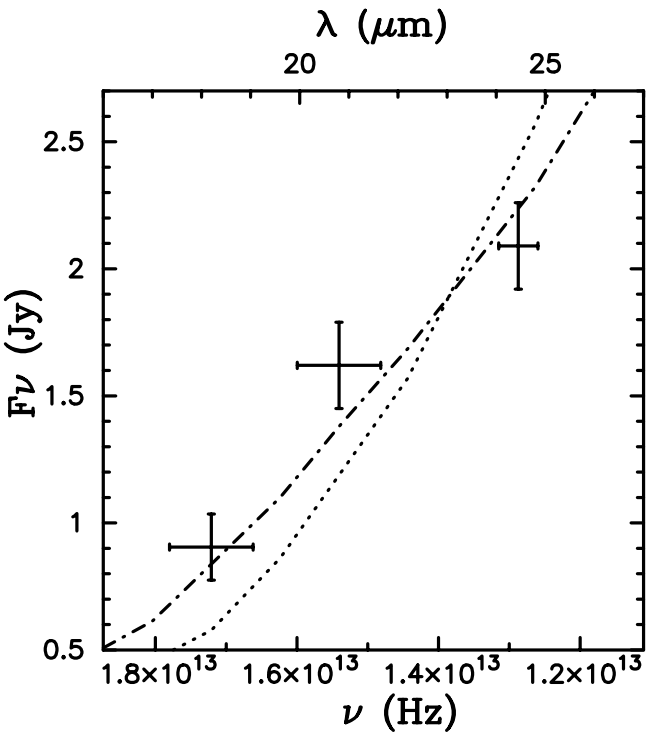

FIG. 7.—Flux densities of HR 4796A at $\lambda = 18.2$, 20.8, and 24.5 μm from Table 1, shown with error bars. The dash-dotted line represents the total SED from the two-component outer-ring model. The dotted line represents the total SED from the single outer-ring model.

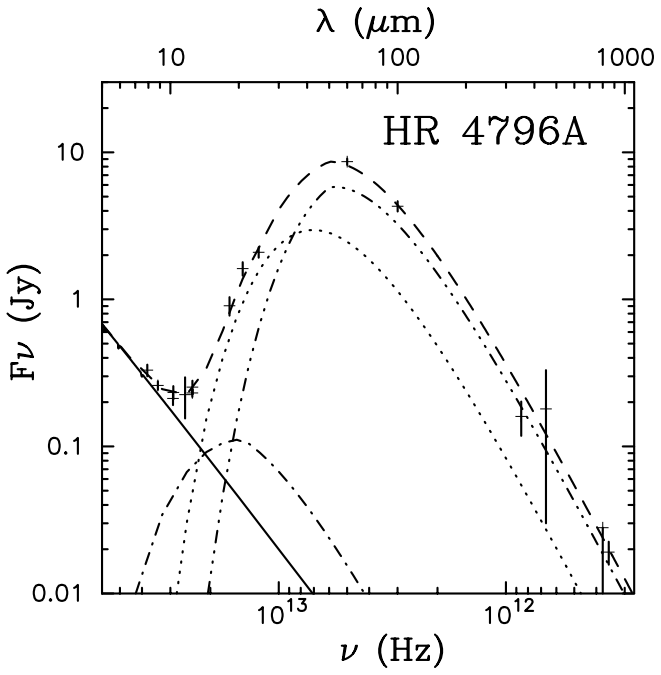

FIG. 8.—Flux densities of HR 4796A from Table 1. Wideband photometry is ignored where narrowband photometry is available. The dashed line represents the total SED from the best-fit two-component outer-ring model. The solid line is the contribution from the photosphere (derived from Kurucz 1993 model). The dotted line is the contribution from the wide outer-ring component. The triple-dot–dashed line is the contribution from the narrow outer-ring component. The dash-dotted line is the contribution from the inner zodiacal dust component.

TABLE 2
UNREDUCED χ^2 FROM FITS TO EACH DATA SET FOR THE SINGLE OUTER RING MODEL AND THE TWO-COMPONENT OUTER RING MODEL

Model	24.5 μm	20.8 μm	12.5 μm	1.1 μm	SED	Total
Number of data points.....	13	12	12	53	16	106
Two-component χ^2	13	15	14	53	15	110
One-component χ^2.....	19	16	22	70	27	154

NOTES.—The top row of the table shows the number of data points in each data set. The next two rows show the corresponding χ^2 values for each model. The single outer ring model (one component) had nine parameters, while the two-component model had 13 parameters. According to the BIC, which takes into account the total unreduced χ^2 values for each model and the number of data points and free parameters, the two-component model is statistically preferred to a significant degree (see details in text). The χ^2 values have been rounded to the nearest integer.

3.2. *An Outer Ring with Two Components*

To date, the wide variety of published imaging and photometric measurements of HR 4796A have not been used simultaneously to constrain model simulations. An oft-used single-ring model fits some of the individual images plausibly well. Here, however, we show that a more complicated model of the outer ring is required to fit all available data. We first find the single-ring model that provides the best simultaneous fit to all data, including Keck/MIRLIN images, the *HST*-NICMOS/NIR image, and all extant flux density measurements of HR 4796A (Table 1). We assume flux values for the zodiacal contribution that were estimated in the previous section; since these contribute negligibly to the other data, only outer-ring parameters are varied. For the coronagraphic *HST*/NICMOS image, a circular region of radius 0.″6 centered on the star is masked, so that only the ansae of the outer ring are considered. This accords with S99, who point out that emission inside this region is largely an artifact of photospheric light scattered off the inner edge of the coronagraphic hole. In image fitting, models are freely scaled and thus only fit to the intensity pattern of the data. The total fluxes at the imaging wavelengths are fit as part of the SED.

To minimize the number of free parameters, we make one additional simplification at the onset of detailed modeling. Searches for best-fit images revealed that the northeast ansae should have an optical depth that is 20% greater than the southwest ansae's optical depth. So we incorporate this asymmetry into all our models by introducing a sinusoidal azimuthal variation into the optical depth description, such that the function has a crest at the northeast peak and a trough at the southwest peak. The amplitude of this azimuthal variation is kept constant across all model fits, thus ridding us of one free parameter.

The inadequacy of the single-ring model is most evident in comparison with images at $\lambda = 12.5$ and 1.1 μm and in a discrepancy between model and observed fluxes at thermal IR wavelengths. In Figure 5*c*, the best-fit single-ring model fails to simulate the extended emission in the 12.5 μm image (Fig. 5*a*). It is also discrepant with the MIR flux densities, as evident in Figure 7. Finally, emission profiles at 1.1 μm (*solid line*) in Figure 6 are not well matched by a single-ring model (*dot-dashed line*) fit to all data. The peaks of model emission are offset toward the star, and model flux is too high at the outer radius and too low at the inner edge. This mismatch is consistent with the positional offset between peaks of scattered-light and thermal emission in Figure 6*b* of T00, an overlay of the *HST*/NICMOS contour map on a 18.2 μm Keck/OSCIR image of HR 4796A. However, it was unclear whether this effect was simply due to the higher temperature at the inner edge of a single outer ring. Evidence outlined above indicates the discrepancy in peak locations is also a consequence of a more complex dust distribution.

Some hints as to how the model can be improved are evident in fits to some of the images. A single uniform-density ($\gamma = 0$) ring model fitted to the MIR images alone gives outer-ring widths of $\sim$60 AU and grain radius of $\sim$5 μm. This is close to the grain radius estimates of T00, where the chief constraint is the relative brightnesses of the outer disks at 10 and 18 μm.

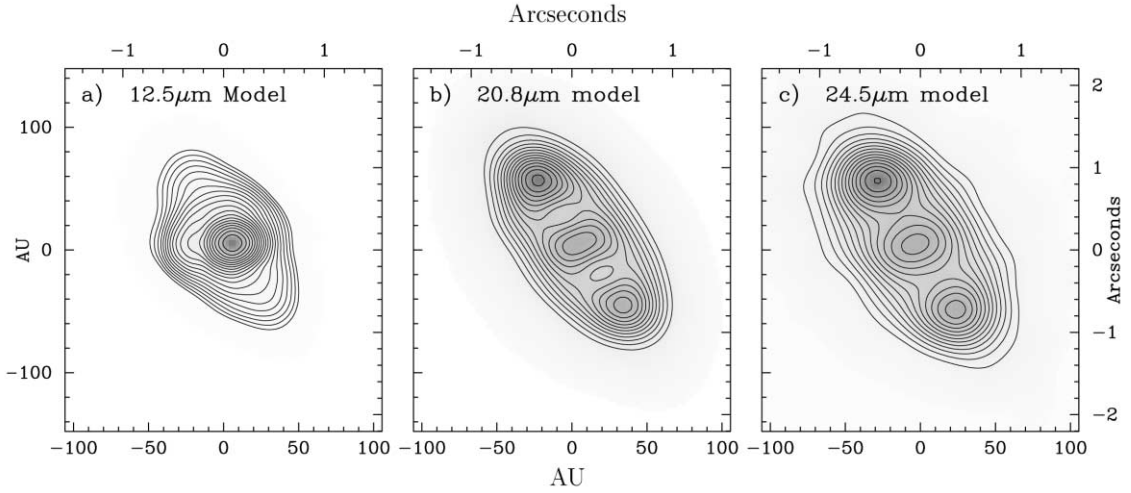

FIG. 9.—Simulated images from the best-fit two-component outer-ring model at the same wavelengths as in Fig. 1. (*a*) Simulation of emission at 12.5 μm. (*b*) Simulation of emission at 20.8 μm. (*c*) Simulation of emission at 24.5 μm. The contour levels for each figure are the same as those in Fig. 1.

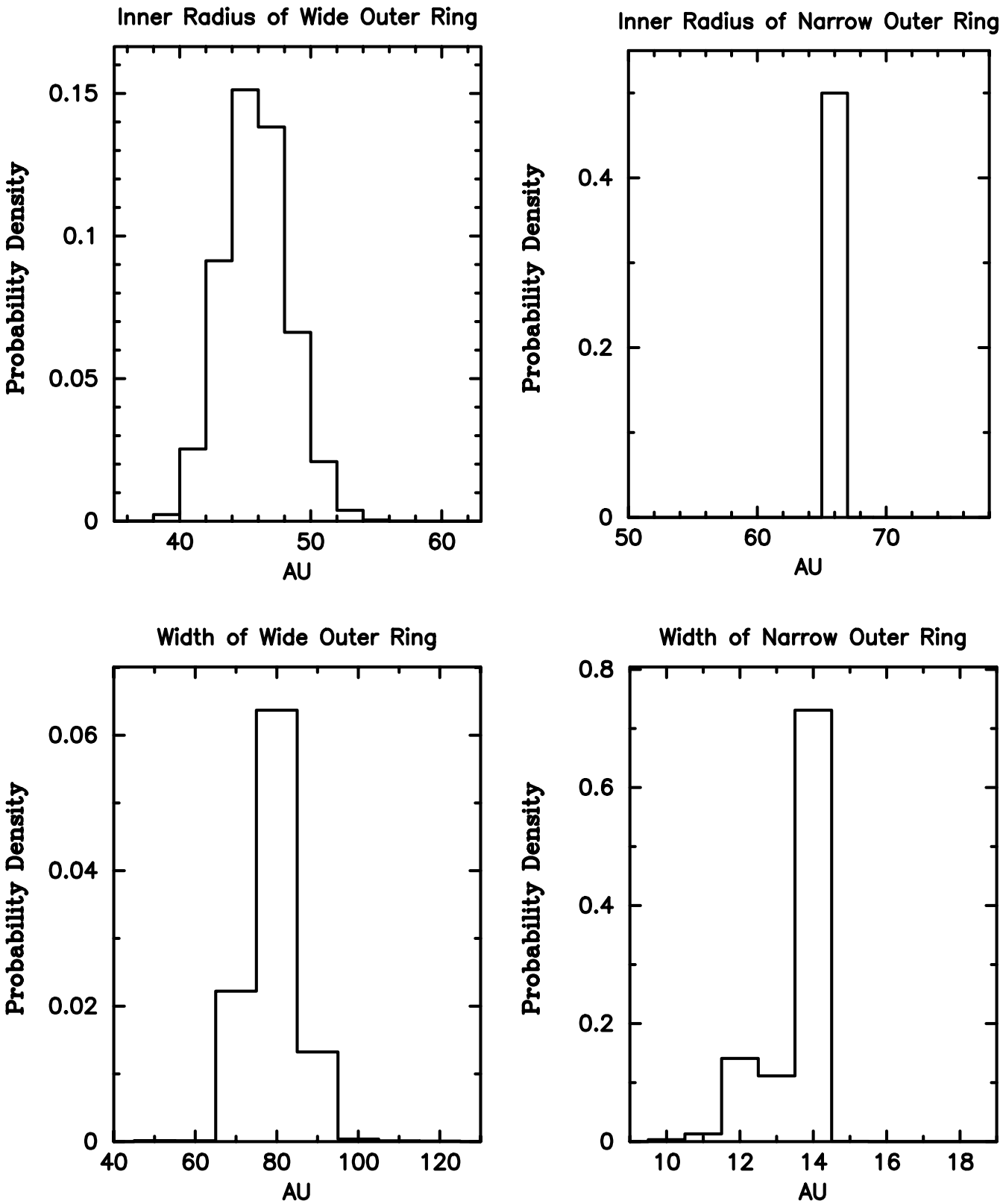

FIG. 10.—Probability distributions for selected two-component outer-ring model parameters. Most probable values correspond to peaks in the probability distributions. The uncertainties are estimated as the 66% confidence intervals (where our distributions are binned finely enough), or the shortest range of parameter values that encompasses 66% of the total probability. The most probable values and uncertainties for these parameters are detailed in the text.

On the other hand, fits to the SED alone yield a 180 AU wide ring with roughly 16 μm grains. Smaller disk sizes yield larger grain sizes. In fact, the Wien side of the outer disk's SED demands small grain sizes, while the Rayleigh-Jeans side of the outer disk's SED (the submillimeter flux densities) demands large grain sizes. Independent fits to the *HST*/NICMOS image yield a narrower ring, however, $\sim$17 AU. These discrepancies suggest that the outer ring has more than one component and that it might be better approximated as two rings, each with a different characteristic grain size.

Comparisons of the two-component outer ring model with the single outer-ring model and data are shown in Figures 5, 6, and 7. The entire SED from the best-fit two-component model is shown in Figure 8. In all cases significant improvements are evident. However, for a more robust quantitative analysis of which model is preferred, we can employ the Bayesian information criterion (BIC) (Liddle 2004; Mukherjee et al. 1998; Jeffreys 1961). This is a model selection criterion that penalizes models for having extra parameters: $\mathrm{BIC} = -2 \ln L + k \ln N$, where L is the likelihood function $e^{-1/2\Sigma_n \chi_n^2}$, k is the number of free parameters, and N is the number of data points. The model with the lower BIC is preferred. A difference of 2 between BICs indicates positive evidence against the high-BIC model, while a difference of 6 indicates strong evidence. The top row in Table 2 shows the number of data points for each of the data sets (images and flux measurements). The next two rows show the unreduced χ^2 values (rounded to the nearest integer) for each of the data sets from the two best-fit models; k for the one-component model is 9, while k for the two-component model is 13. From these numbers, the BIC for the one-component model is 196, and the BIC for the two-component model is 171. The magnitude of this difference provides strong evidence that a two-component model is mandated by the data.

The best-fit model (two-component outer ring) is shown at MIR wavelengths in Figure 9. Single-ring best-fit parameters are $R_{\rm in} = 64 \pm 4$ AU, $\Delta R = 80 \pm 6$ AU, $\gamma = 4.88 \pm 0.2$, $\lambda_0 = 31 \pm 3$ μm ($a = 21$ μm), $\sigma = (3.3 \pm 0.2) \times 10^{-3}$, and albedo $= 0.3 \pm 0.02$. Uncertainties were estimated through the Bayesian approach. The two-component outer-ring model parameters are $R_{\rm in\,1} = 45 \pm 5$ AU, $\Delta R_1 = 80 \pm 15$ AU, $\lambda_{01} = 5 \pm 2$ μm ($a_2 = 3.3$ μm), $\sigma_1 = (2.1 \pm 0.2) \times 10^{-3}$ (implying a total cross-sectional area of 90 AU^2), and albedo $\omega_1 = 0.35 \pm 0.03$, and $R_{\rm in\,2} = 66 \pm 1$ AU, $\Delta R_2 = 14 \pm 1$ AU, $\lambda_{02} = 38 \pm 5$ μm ($a = 25$ μm), $\sigma_2 = (3.8 \pm 0.25) \times 10^{-2}$ (implying a total cross-sectional area of 245 AU^2), and albedo $\omega_2 = 0.18 \pm 0.02$. The γ-parameter was not used for either ring. The probability distributions, obtained by the Bayesian approach, for some of these parameters are shown in Figure 10.

4. DISCUSSION

Analysis of multiwavelength HR 4796A images and flux densities yields a refined estimate of the properties of its circumstellar dust as follows. Radial structure of the outer ring is best approximated by two components: a narrow ring of $\sim$50 μm grains between 66 and 80 AU, and a surrounding wider ring of $\sim$7 μm grains stretching from 45 to about 125 AU. The presence of excess emission at the stellar position is confirmed. It is unresolved by a 0.″37 FWHM PSF (corresponding to a 12.5 AU radius at the 67 pc distance of HR 4796A) and has a temperature of $\sim$260 K. Bayesian parameter estimation suggests this dust is $\sim$4 AU from the star with a total grain cross-sectional area of 0.055 AU^2.

4.1. *Exozodiacal Dust*

Evidence for warm exozodiacal dust was first identified for HD 98800 (Zuckerman & Becklin 1993). This K dwarf quadruple system of two spectroscopic binaries (Torres et al. 1995) exhibits one of the strongest dust signatures of any in the *IRAS* catalog. Its IR excess peaks at 25 μm and is associated entirely with the northern spectroscopic binary, HD 98800 B (Koerner et al. 2000). Modeling of the SED of the dust suggests a ring of particles in the few micron size range with an inner radius of a few AU and an outer radius that may stretch well into a giant-planet zone. Subsequent detections of warm excess from the main-sequence A3 star, ζ Lep, have also been interpreted as originating from collision in an asteroid belt (Chen & Jura 2001).

The origin of a warm component to circumstellar dust around HR 4796A may be similar to that of our own solar system. Zodiacal dust is supplied predominantly by the asteroid belt, Jupiter family comets (JFCs), long-period comets, and perhaps by dust from the Kuiper Belt and the Oort Cloud (Flynn 1994; Dermott et al. 1992; Durda & Dermott 1992; Liou & Dermott 1993). At 1 AU, about 45% of the dust in the ecliptic plane is believed to come from the asteroid belt and JFCs. Within a sphere of radius 1 AU, however, 89% of the dust is from comets. The fractional surface density of zodiacal dust grains is $\sigma(r) \sim r^{-1.45}$ (Hahn et al. 2002), with grain sizes as large as 100 μm (Grogan et al. 2001).

An asteroid belt may be the source of exozodiacal dust grains around HR 4796A. Their total grain cross section of $\sim$0.055 AU^2 and effective grain size of 28 μm yields a minimum mass of $\sim 10^{-3}$ $M_\oplus$, under the assumption that the grain density is given by $\rho = 2500$ kg m^{-3} (Jura et al. 1998). Ice sublimation occurs instantaneously at 4 AU from the star (Isobe 1970), so these grains are almost certainly refractory. The blowout size due to radiation pressure is 7 μm (calculated according to Backman & Paresce 1993; Gustafson 1994) and indicates that this is not an effective dispersal mechanism for the grains we detect. Because of relatively high fractional surface density ($\sigma = 0.0046$), the collisional lifetime is shorter than the Poynting-Robertson lifetime, even at 4 AU. Grains are primarily being destroyed by collisions but probably also originate in a cascade of collisions from larger bodies. Assuming a grain size distribution, $n(a) \sim a^{-3.5}$, and 1000 km planetesimals for the largest bodies, the total mass of orbiting material is $\sim$0.6 $M_\oplus$.

Another possible source for HR 4796A's exozodiacal dust is a more distant asteroid or exo-Kuiper belt. Grains may spiral in toward the star under the influence of Poynting-Robertson drag but be trapped by resonant interactions with terrestrial planets. The dust may come only from more tenuous parts of the disk where collisional destruction is not the dominant dispersal phenomenon. For our solar system, however, Liou et al. (1996) showed that Kuiper Belt grains in the range 9–50 μm are unlikely to survive collisions with interstellar grains (as opposed to interplanetary grains) on their way to the Sun, and 80% of all migrating grains are likely to be thrown out of the solar system by interactions with the giant planets. However, dust can be trapped in planets interior to an asteroid belt, and in these cases grains roughly 30 μm or greater in size seem to be the best candidates (Jackson & Zook 1992). Large asteroid grains can even be injected into interior resonances with exterior planets because of the initial outward thrust of radiation pressure upon their release from a parent body. As they leave these resonances they usually have lower eccentricities and orbital inclinations that

render them susceptible to capture in resonant orbits with interior planets.

Comets that travel close to the star may provide a source of exozodiacal dust grains around HR 4796A. The cometary component of zodiacal dust is thought to be highly variable, according to simulations done by Napier (2001), and may increase the dust creation rate from 100- to 1000-fold within periods of 100,000–10,000 yr. Particles that are most likely to be trapped in our own solar system have sizes between 10 and 100 μm (Jackson & Zook 1992). Dust grains with low eccentricities and low orbital inclinations are again more likely to be captured in resonant orbits. It should be noted that while the radiation pressure blowout size for the solar system is roughly 0.9 μm, it is 7 μm for HR 4796A. The optical depth of the zodiacal dust at 25 μm is roughly 10^{-7} when measured along the ecliptic (Spiesman et al. 1995). For HR 4796A, assuming similar dust dispersal timescales, this would imply a dust production rate roughly 10^4 times higher than expected for the solar system. Grain velocities also differ in the two systems. Thus, it is best to undertake system-specific simulations before speculating too much about the origin of exozodiacal dust grains. Regardless of origin, the main explanation for the persistence of dust in the exozodiacal region is probably resonance trapping by interior planets as found in the solar system.

4.2. *Properties of HR 4796A's Outer Ring*

A cold, massive outer ring of dust particles is more readily detected around stars other than the Sun. Examples other than HR 4796A include Fomalhaut (Holland et al. 1998), ϵ Eri (Greaves et al. 1998), and Vega (Holland et al. 1998; Koerner et al. 2001; Wilner et al. 2002). However, such a structure is more difficult to detect in our own solar system, where confusion from the inner zodiacal dust interferes with emission from outer dust grains (Backman et al. 1998). The discovery of a sizeable aggregation of Kuiper Belt objects (see review by Luu & Jewitt 2002) implies an associated population of dust grains (Backman et al. 1995). Larger grains are likely to be better retained in the Kuiper Belt region by mean motion resonances, while smaller grains diffuse under the influences of Poynting-Robertson drag, solar wind drag, and radiation pressure (Holmes et al. 2003).

The *HST*/NICMOS image of HR 4796A at 1.1 μm establishes that most of the scattered light around HR 4796A arises within a 17 AU ring centered at 70 AU (S99). A wider low-density component is also needed to fit Keck/MIRLIN images of thermal emission. The SED can be fitted by a single narrow ring, but only if the large-grain contribution to the size distribution is boosted significantly. LL03 used $n(a) \sim a^{-2.9}$ to do this, but their models fail to match the surface brightness distribution in thermal IR images. Inclusion of two distinct effective grain sizes resolves an apparent inconsistency in the interpretation of different data sets. Thermal IR images modeled by T00 required small grains ($\sim$3 μm), but a fit by K98 that included an upper limit to the flux density at 800 μm required the presence of large grains ($\sim$30 μm) to fit the Rayleigh-Jeans side of the SED. The latter result is confirmed here by fits that include more recent detections of emission at 450 and 800 μm (Holland et al. 1998) and a new measurement at 350 μm. A two-part ring with separate grain-size distributions is necessary to reproduce observations at *all* wavelengths.

Properties derived here for HR 4796A's outer ring are consistent with theoretical predictions for both our solar system's outer dust and for exo-Kuiper grains in general. The collision of large planetesimals is expected to produce a cascade of smaller sized particles with number distribution $dn(a)/da \sim a^{-3.5}$ (Dohnanyi 1969). Subsequent grain evolution is affected largely by radiation pressure; Poynting-Robertson drag is a relatively small effect. Radiation pressure effects can be parameterized by β:

$$\beta(D) = (1150/\rho D)(L_*/L_\odot)(M_\odot/M_*),$$

where D is grain diameter in μm and ρ is grain density in SI units (Gustafson 1994; W99). Appropriate values for HR 4796A are $M_* = 2.5\ M_\odot$ (Jura et al. 1998) and $\rho = 2500$ kg m^{-3} and yield $\beta(D) = 3.5/D$. Large particles with $D > 35$ correspond to $\beta < 0.1$ and will remain in original orbits close to parent bodies. Grains in the size range 35 μm $> D >$ 7 μm are "β-critical," with values $0.1 < \beta < 0.5$. These experience orbital evolution, which extends their distribution both inward and outward. The smallest grains ($D < 7$ μm and $\beta > 0.5$) have been called "β-meteoroids" and are blown out of the system on hyperbolic orbits.

This picture of grain evolution provides a natural explanation for the properties of the outer ring around HR 4796A. In this scenario, a large-grain ring centers on a system of planetesimals surrounded by an outer region of smaller grains diffused under the influence of radiation pressure. Large grains in the narrow ring have $\beta < 0.1$, $D > 35$ μm, or $D \sim 50$ μm in our model, so they stay close to parent bodies. Smaller grains are β-critical or β-meteoroids, since their size is so close to the 7 μm ($D \sim 6.6$ μm) threshold. However, β-critical is more likely, since β-meteoroids have a "blowout" lifetime of order 100 yr, while β-critical dust has a collisional lifetime of order 1000 yr. This idea is supported by comparison with expected size distributions. The large- and small-grain populations have a diameter ratio of about 7:1 and cross-sectional areas 90 AU^2 for small grains and 245 AU^2 for large grains. So the number of grains is approximately 20:1 for small:large grains. In contrast, the initial ratio for a collisionally generated size distribution should be $(7/50)^{-3.5} \sim 1000$:1. This underabundance of small grains agrees well with the hypothesis that many β-meteoroids have already left the system.

4.3. *Further Work*

The modeling approach presented in this work was designed to determine the simplest disk morphology required by observations with a minimum number of underlying assumptions. The resulting dust distribution suggests significant physical interpretations. These should be tested with a more complex analysis that uses a more realistic representation of dust grain properties, including physically meaningful size distributions and plausible assumptions about grain composition. The latter should in turn be coupled to models that simulate the dynamical evolution of dust grains under the influence of planetary bodies in the HR 4796A system.

Further progress in observing HR 4796A's radial dust distribution will be difficult until a next generation of large-aperture telescopes comes online, since Keck/MIRLIN images are already close to the diffraction limit of a 10 m telescope. ALMA may provide submillimeter images with resolution improved by a factor of 5. The next-generation telescopes, such as the 30 m "Giant Segmented Mirror Telescope," the "Thirty Meter Telescope," and the 100 m "Overwhelmingly Large Telescope,"

will have also improved resolution and greatly enhanced sensitivity, and high dynamic range techniques that are designed to search for planets may provide more detail on reflected light. Meanwhile, progress in observations of exozodiacal and exo-Kuiper dust configurations may be better advanced by studying systems that are closer than the 67 pc distance to HR 4796A. The enhanced sensitivity of the *Spitzer Space Telescope* will identify nearby debris-disk systems for which spatial resolution will be improved. Nulling interferometers (Keck and LBT) will also bring enhanced capability to study their inner-dust regions. Ultimately, coordinated planet searches will be able to verify the relationship between circumstellar dust signatures and the presence of a planetary system.

Portions of this work were carried out at the Jet Propulsion Laboratory, which is operated by the California Institute of Technology under a contract with NASA. Data presented herein were obtained at the W. M. Keck Observatory, which is operated as a scientific partnership among the California Institute of Technology, the University of California, and the National Aeronautics and Space Administration. The Observatory was made possible by the generous financial support of the W. M. Keck Foundation. The authors wish also to recognize and acknowledge the very significant cultural role and reverence that the summit of Mauna Kea has always had within the indigenous Hawaiian community. We are most fortunate to have the opportunity to conduct observations from this mountain.

REFERENCES

Artymowicz, P., Burrows, C., & Paresce, F. 1989, ApJ, 337, 494
Augereau, J. C., Lagrange, A. M., Mouillet, D., & Ménard, F. 1999, A&A, 350, L51
Backman, D. E., Caroff, L. D., Sandford, S. A., & Wooden, D. H., eds. 1998, Conf. Proc. Exozodiacal Dust Workshop (NASA CP-1998-10155; Moffett Field: NASA Ames Research Center)
Backman, D. E., Dasgupta, A., & Stencel, R. E. 1995, ApJ, 450, L35
Backman, D. E., Gillett, F. C., & Witteborn, F. C. 1992, ApJ, 385, 670
Backman, D. E., & Paresce, F. 1993, in Protostars and Planets III, ed. E. H. Levy & J. I. Lunine (Tucson: Univ. Arizona Press), 1253
Chen, C. H., & Jura, M. 2001, ApJ, 560, L171
Dermott, S. F., Durda, D. D., Gustafson, B. A. S., Jayaraman, S., Xu, Y. L., Gomes, R. S., & Nicholson, P. D. 1992, in Asteroids, Comets, Meteors 1991, ed. A. Harris & E. Bowell (Washington, DC: NASA), 153
Dermott, S. F., Jayaraman, S., Xu, Y. L., Gustafson, B. A. S., & Liou, J. C. 1994, Nature, 369, 719
Diner, D. J., & Appleby, J. F. 1986, Nature, 322, 436
Dohnanyi, J. 1969, J. Geophys. Res., 74, 2531
Durda, D. D., & Dermott, S. F. 1992, BAAS, 24, 951
Fajardo-Acosta, S. B., Telesco, C. M., & Knacke, R. F. 1998, AJ, 115, 2101
Flynn, G. J. 1994, Lunar Planet. Sci. Conf., 25, 379
Gillett, F. C. 1986, in Light on Dark Matter: Proc. First Infra-Red Astronomical Satellite Conference, ed. F. P. Israel (Dordrecht: Reidel), 61
Greaves, J. S., et al. 1998, ApJ, 506, L133
Greenberg, J. M. 1978, in Infrared Astronomy, ed. G. Setti & G. G. Fazio (NATO ASI Ser. C38; Dordrecht: Reidel), 51
Grogan, K., Dermott, S. F., & Durda, D. D. 2001, Icarus, 152, 251
Gustafson, B. A. S. 1994, Annu. Rev. Earth Planet. Sci., 22, 553
Hahn, J. M., Zook, H. A., Cooper, B., & Sunkara, B. 2002, Icarus, 158, 360
Holland, W. S., et al. 1998, Nature, 392, 788
———. 1999, MNRAS, 303, 659
Holmes, E. K., et al. 2003, ApJ, 597, 1211
Houk, N., & Sowell, J. 1985, BAAS, 17, 878
Isobe, S. 1970, PASJ, 22, 429
Jackson, A. A., & Zook, H. A. 1992, Icarus, 97, 70
Jayawardhana, R., Fisher, S., Hartmann, L., Telesco, C., Piña, R., & Giovanni, F. 1998, ApJ, 503, L79 (J98)
Jeffreys, H. 1961, Theory of Probability (3rd ed.; Oxford: Oxford Univ. Press)
Jura, M., Ghez, A. M., White, R. J., McCarthy, D. W., Smith, R. C., & Martin, P. G. 1995, ApJ, 445, 451
Jura, M., Malkan, M., White, R., Telesco, C., Piña, R., & Fisher, R. S. 1998, ApJ, 505, 897
Jura, M., Zuckerman, B., Becklin, E. E., & Smith, R. C. 1993, ApJ, 418, L37
Koerner, D. W., Jensen, E. L. N., Cruz, K. L., Guild, T. B., & Gultekin, K. 2000, ApJ, 533, L37
Koerner, D. W., Ressler, M. E., Werner, M. W., & Backman, D. E. 1998, ApJ, 503, L83 (K98)
Koerner, D. W., Sargent, A. I., & Ostroff, N. A. 2001, ApJ, 560, L181
Kurucz, R. L. 1993, CD-ROM 13, ATLAS9 Stellar Atmosphere Programs and 2 km/s Grid (Cambridge: SAO)
Lay, O. P., Carlstrom, J. E., & Hills, R. E. 1997, ApJ, 489, 917
Li, A., & Lunine, J. I. 2003, ApJ, 590, 368 (LL03)
Liddle, A. R. 2004, MNRAS, 351, L49
Liou, J.-C., & Dermott, S. F. 1993, in Abstracts for IAU Symp. 160, Asteroids, Comets, Meteors 1993 (Houston: Lunar Planet. Inst.), 191
Liou, J.-C., Zook, H. A., & Dermott, S. F. 1996, Icarus, 124, 429
Luu, J. X., & Jewitt, D. C. 2002, ARA&A, 40, 63
Mukherjee, S., Fiegelson, E. D., Babu, G. J., Murtagh, F., Fraley, C., & Raftery, A. 1998, ApJ, 508, 314
Nakano, T. 1988, MNRAS, 230, 551
Napier, W. M. 2001, MNRAS, 321, 463
Ressler, M. E., Werner, M. W., Van Cleve, J., & Chou, H. A. 1994, Exp. Astron., 3, 277
Schneider, G., et al. 1999, ApJ, 513, L127 (S99)
Sitko, M. L., Lynch, D. K., & Russell, R. W. 2000, AJ, 120, 2609
Spiesman, W. J., et al. 1995, ApJ, 442, 662
Stauffer, J. R., Hartmann, L. W., & Barrado y Navascues, D. 1995, ApJ, 454, 910
Telesco, C. M., et al. 2000, ApJ, 530, 329 (T00)
Torres, C. A. O., Quast, G., de La Reza, R., Gregorio-Hetem, J., & Lepine, J. R. D. 1995, AJ, 109, 2146
Wahhaj, Z., Koerner, D. W., Ressler, M. E., Werner, M. W., Backman, D. E., & Sargent, A. I. 2003, ApJ, 584, L27
Weinberger, A. J., Becklin, E. E., & Zuckerman, B. 2003, ApJ, 584, L33
Wilner, D. J., Holman, M. J., Kuchner, M. J., & Ho, P. T. P. 2002, ApJ, 569, L115
Wyatt, M. C., Dermott, S. F., Telesco, C. M., Fisher, R. S., Grogan, K., Holmes, E. K., & Piña, R. K. 1999, ApJ, 527, 918 (W99)
Zuckerman, B., & Becklin, E. E. 1993, ApJ, 406, L25